nature astronomy

LETTERS

https://doi.org/10.1038/s41550-020-01287-8

High-energy emission from a magnetar giant flare in the Sculptor galaxy

The Fermi-LAT Collaboration*

Magnetars are the most highly magnetized neutron stars in the cosmos (with magnetic field 10^{13}–10^{15} G). Giant flares from magnetars are rare, short-duration (about 0.1 s) bursts of hard X-rays and soft γ rays[1,2]. Owing to the limited sensitivity and energy coverage of previous telescopes, no magnetar giant flare has been detected at gigaelectronvolt (GeV) energies. Here, we report the discovery of GeV emission from a magnetar giant flare on 15 April 2020 (refs. [3,4] and A. J. Castro-Tirado et al., manuscript in preparation). The Large Area Telescope (LAT) on board the Fermi Gamma-ray Space Telescope detected GeV γ rays from 19 s until 284 s after the initial detection of a signal in the megaelectronvolt (MeV) band. Our analysis shows that these γ rays are spatially associated with the nearby (3.5 megaparsecs) Sculptor galaxy and are unlikely to originate from a cosmological γ-ray burst. Thus, we infer that the γ rays originated with the magnetar giant flare in Sculptor. We suggest that the GeV signal is generated by an ultra-relativistic outflow that first radiates the prompt MeV-band photons, and then deposits its energy far from the stellar magnetosphere. After a propagation delay, the outflow interacts with environmental gas and produces shock waves that accelerate electrons to very high energies; these electrons then emit GeV γ rays as optically thin synchrotron radiation. This observation implies that a relativistic outflow is associated with the magnetar giant flare, and suggests the possibility that magnetars can power some short γ-ray bursts.

On 15 April 2020, the Fermi Gamma-ray Burst Monitor (GBM) triggered and located γ-ray burst (GRB) 200415A[4], which was initially classified as a short (duration <2 s) γ-ray burst (SGRB). The Interplanetary Network of γ-ray detectors (IPN, http://ssl.berkeley.edu/ipn3/index.html) reduced the uncertainty on the GBM position to 20 square arcmin, suggesting that the GRB originated from the nearby Sculptor galaxy[3], located at a distance of about 3.5 megaparsecs[5]. This, with the resemblance of the GBM sub-MeV light curve (E. Burns, manuscript in preparation) to the extragalactic soft gamma repeater (SGR) giant flare candidates GRB 051103[3,6] and GRB 070201[7], and the detection of quasi-periodic oscillations by the Atmosphere–Space Interaction Monitor (A. J. Castro-Tirado et al., manuscript in preparation), led to the identification of GRB 200415A as a magnetar giant flare (MGF) in Sculptor. GRB 200415A was 43° from the LAT boresight at the GBM trigger time T_0 (08:48:05.563746 UTC) and remained well within the LAT field of view (FOV) until 500 seconds after T_0. Three γ rays were detected by the LAT, allowing the localization of GRB 200415A at high energies (>100 MeV): this detection of high-energy γ-ray emission from an MGF suggests that magnetars can power the relativistic outflows observed in some SGRBs.

To study the localization of the γ-ray signal observed by the LAT we perform a likelihood analysis and compute a test statistic (TS) for the presence of the source at different positions. The best position is obtained from the maximum of the TS ($TS_{max} = 29$, corresponding to a detection significance close to 5σ; see the Methods and Extended Data Fig. 1 for the numerical value of the best-fit model). Then, the variation of the TS around this position provides the map of localization contours shown in Fig. 1. The iso-contours in red encompass localization probabilities of 68% and 90%.

Four galaxies (IC 1576, IC 1578, IC 1582 and NGC 253) from the NGC 2000 catalogue[8] are located within a circular region of radius r_{99}, whose area is equivalent to the 99% confidence level, and which is centred on the maximum of the TS map at right ascension (RA) = 11.13° and declination (dec.) = −24.97° (J2000). NGC 253, also known as the Sculptor galaxy, has already been detected as a steady source in γ rays[9,10] with a flux integrated between 100 MeV and 100 GeV of $(1.3 \pm 0.2) \times 10^{-8}$ cm^{-2} s^{-1}. The γ-ray emission is powered by cosmic rays accelerated by supernova remnants interacting with the interstellar gas, and the enhanced massive star-formation activity in the galaxy also favours the presence of stellar remnants like magnetars. The centre of the galaxy lies on the contour containing a localization probability of 72%.

We apply the likelihood ratio (LR) method[11] to quantify the reliability of a possible association of the γ-ray source with Sculptor. This method can distinguish between two situations: the true counterpart associated with a γ-ray emitter, which appears to lie a certain distance away owing to localization uncertainties; or a background object which, by chance, happens to lie close to the γ-ray position. Our analysis takes into account the angular size of the counterpart candidate and the elongated shape of the LAT localization contours shown in Fig. 1. Since the LR method takes into account the magnitude of the galaxy, we find that the Sculptor galaxy is the most likely host galaxy of the source detected by the LAT with a LR value approximately 60 times larger than the values for other galaxies. To evaluate the statistical significance of this association, we compare the LR values obtained in these analyses with the same analyses repeated over a sample of random locations in the sky. The P values range from 3.2×10^{-4} to 2.9×10^{-3} depending on the particular analysis (see details in the Methods and Extended Data Figs. 3 and 4). Both analyses suggest a positional association between Sculptor and the LAT γ-ray detection. Assuming that the emission detected by the LAT is from an SGRB, our calculation of the false alarm rates (FARs) ranges from 5.4×10^{-4} yr^{-1} to 4.7×10^{-3} yr^{-1}.

We perform a detailed maximum likelihood spectral analysis of the LAT emission by modelling GRB 200415A as a point source with a power-law spectrum. As part of our analysis we estimate the probability that each photon detected by the LAT is associated with the point source, as opposed to any of the other model components. The list of events is shown in Extended Data Fig. 2. Three events are associated with the source with a probability greater than 90%. The arrival times (after T_0) of these events are 19 s, 180 s and 284 s, with

*A list of authors and their affiliations appears at the end of the paper.

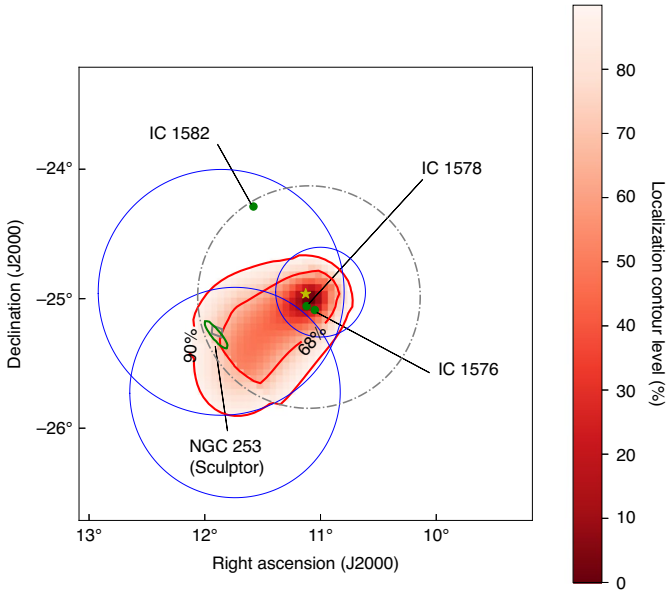

Fig. 1 | Map of the localization contour probability. The contours encompassing a probability of 68% and 90% are displayed in red, while the yellow star marks the location of the TS maximum. Galaxies from the NGC 2000 catalogue are shown as green disks, except for NGC 253 (Sculptor galaxy), which is shown as an extended source. The grey box indicates the localization provided by the IPN[3]. The circle whose area is equivalent to the 99% confidence level is displayed with a grey dashed-dotted line, while the blue circles indicate the 68% containment of the point spread function (PSF) for the three γ rays probably associated with the flare.

energies 480 MeV, 1.3 GeV and 1.7 GeV, respectively. The reconstructed directions of these events are shown in Fig. 1 as circles with a radius equal to the PSF of the instrument at their respective energies. To estimate the significance of this cluster of three events (triplet) and the probability that it is due to a background fluctuation, we look at a region of 1° radius around the location of Sculptor using the entire LAT dataset available (more than 12 years of data). Two different analyses, applying that of Li and Ma[12] and Bayesian blocks (BB) methods[13,14], result respectively in P values of $P_{\rm Li\&Ma} = 8.3\times10^{-7}$ and $P_{\rm BB} = 2.3\times10^{-3}$. See Methods for details, as well as Extended Data Figs. 5 and 6. Finally, we calculate the rate of chance coincidence between a LAT triplet signal and a GBM SGRB in the same region of Sculptor within a given time window. The FARs for the two analyses are $1.6\times10^{-7}\,{\rm yr}^{-1}$ and $6.3\times10^{-8}\,{\rm yr}^{-1}$ respectively.

To summarize, the FAR of detecting high-energy emission from an SGRB spatially associated by chance to Sculptor is one event in approximately 200–1,800 years, depending on the analysis method, while the FAR of the event also being temporally coincident with a GBM SGRB is of the order of one event every 10^6–10^7 yr. Accordingly, we conclude that the LAT signal is associated with an MGF event in Sculptor.

The intense GBM emission below 1 MeV defines the so-called 'initial spike' of the MGF and must come from a relativistic wind[4]. The three local magnetars that have displayed MGFS (two in the Milky Way and one in the Large Magellanic Cloud) each had pulsating late-time emission of effective temperature 10–25 keV, emitting about 10^{44} erg of energy over a few hundred seconds. The LAT signal cannot come from this region ($R\lesssim3\times10^7$ cm) owing to the high opacity[15] to $\gamma\rightarrow e^+e^-$ pair creation in the magnetar's enormous magnetic field. The long ($t_{\rm del}=19$ s) delay between the initial spike and first LAT photon detection suggests that the GeV emission must take place well outside the light cylinder radius $Pc/2\pi\approx10^{10}$–10^{11} cm for magnetars of rotation periods $P\approx2$–12 s. Thus, the scenario we propose is that the GeV emission arises from dissipation associated with the collision between an ultra-relativistic outflow from the MGF and an external shell of swept-up material. The huge energy release, approximately 10^{47} erg, within about 0.14 s (ref. [4]), probably from magnetically induced crustal fracturing of the magnetar surface[16] or from the deformation of the magnetosphere[17,18], creates a very hot plasma. Initially, the radiation is trapped inside this magnetized plasma rich in electron–positron pairs and vastly fewer baryons. The plasma accelerates under its own radiation pressure and becomes optically transparent to electron scattering at distances $R>10^8$ cm from the magnetar. The emission of radiation from a range of radii and with a range of effective temperatures $\lesssim$300 keV constitutes a Comptonized spectrum peaking at about 1 MeV, as observed by the GBM. The accompanying plasma continues its outward flow with a bulk Lorentz factor $\Gamma_{\rm ej}\approx100$ and kinetic energy of about 3×10^{46} erg (refs. [19,20]). Such a high Lorentz factor is in contrast to the MGFs observed in the Milky Way that powered only mildly relativistic outflows observed as radio nebulae[21,22] expanding at about $0.7c$, where the much lower expansion velocity can be attributed to entrainment of a larger baryon mass. The inferred kinetic energy of the outflow from the MGF in Sculptor is, however, comparable with the total radiated energy in the initial spike, as was also inferred for the previous local MGFs.

In its quiescent state, the magnetar putatively emits a pulsar-type ultra-relativistic magnetohydrodynamic wind powered by its spin-down energy. The continual wind sweeps up interstellar gas, and stalls at a bow shock, forming a shell at a distance $R_{\rm bs}\approx8\times10^{15}$ cm. The MGF outflow, which itself becomes a thin shell over time, therefore propagates essentially inside an evacuated cavity until it collides with the bow-shock shell. The time of collision is approximately $R_{\rm bs}/2\Gamma_{\rm ej}^2c\approx10$ s, which is similar to the time $t_{\rm del}$. After collision, a forward shock propagates inside the bow-shock shell and a reverse shock propagates inside the MGF shell. Electrons are accelerated at the shocks to relativistic energies and emit synchrotron radiation up to GeV energies in shock-generated magnetic fields. The duration of the peak emission is approximately $R_{\rm bs}/2\Gamma_{\rm sh}^2c\approx400$ s, where $\Gamma_{\rm sh}\approx20$ is the bulk Lorentz factor of the forward shock. This is the timescale over which the LAT detected synchrotron photons with energies of up to a few GeV (Methods).

GRB 200415A is an MGF detected at $\gtrsim$100 MeV energies, noting that similarities between the MGFs and cosmological GRBs have been pointed out in the past[2,23,24]. Previous searches in LAT data for persistent hard γ-ray emission from several Galactic magnetars resulted in stringent upper limits[25,26]. The 10–500 seconds (from T_0) LAT spectrum of GRB 200415A, with a photon index $\Gamma=-1.7\pm0.3$ and a flux of $(4.1\pm2.2)\times10^{-6}\,{\rm cm}^{-2}\,{\rm s}^{-1}$ (two orders of magnitude brighter than the non-variable flux of Sculptor), is typical of an SGRB detected by the LAT. What makes GRB 200415A different from other LAT-detected SGRBs is the long delay of about 19 s compared to typical values of $\lesssim$1 s between the GBM trigger time and the LAT detection[27] (Methods). Among the 17 SGRBs detected by the LAT in the first 10 years, GRB 200415A shows the longest delay between the end of the GBM-detected emission and the beginning of the high-energy emission, and only two SGRBs were detected by the LAT for a duration comparable to that of GRB 200415A (see Extended Data Fig. 7). Although these peculiarities by themselves do not rule out GRB 200415A being a cosmological SGRB, its association with Sculptor, its very flat GBM spectrum below 1 MeV (ref. [4]), and the quasi-periodic oscillation detection by the Atmosphere–Space Interaction Monitor (A. J. Castro-Tirado et al., manuscript in preparation) all strongly point toward an MGF origin.

We suggest that an ultra-relativistic outflow with energy similar to the prompt γ-ray energy emanated from the MGF in Sculptor and that this outflow hit a dense shell of material surrounding the magnetar. Shock-heated material accelerated electrons to relativistic

energies, which emitted synchrotron radiation in the presence of a magnetic field generated in the shocks. The GRB 200415A detected by the LAT is thus the high-energy component of the spectrum of an MGF.

Methods

The LAT. The Fermi Gamma-Ray Space Telescope was placed in a low-Earth orbit on June 11, 2008. Its two scientific instruments, the LAT[28] and the GBM[29], together provide the capability of probing emission over several decades in energy. The LAT is a pair production telescope sensitive to γ rays in the energy range from about 30 MeV to more than 300 GeV. Whether or not a γ ray is detected by the LAT is primarily defined by two angles: the angle ζ with respect to the spacecraft zenith, and the viewing angle θ from the LAT boresight. In the analysis performed in this paper, we do not make any explicit cuts on the angle θ; however, the exposure drops very quickly for θ greater than about 75°. When we calculate the exposure and the live time, on the other hand, we only include time intervals when the entire region of interest (ROI) has $\zeta < 100°$ and $\theta < 80°$. The wide FOV (about 2.4 sr at 1 GeV) of the LAT, its high observing efficiency (scanning the entire sky every 3 h), its broad energy range, its large effective area, its low dead time per event (about 27 μs), its efficient background rejection, and its good angular resolution (the 68% containment radius of the PSF is about 0.8° at 1 GeV) are all much better than those of previous instruments. With respect to those instruments, the LAT provides more GRB detections, higher statistics per detection, and more accurate localization. From the second LAT GRB catalogue (2FLGC)[27], the average detection rates for the LAT are 1.7 short GRBs and 17 long GRBs per year.

Detection and localization of the LAT signal. We perform an unbinned maximum likelihood analysis, using LAT `P8_TRANSIENT020E` events within a ROI with a radius of 12° (initially centred on the GBM final ground position[30]). We select a time interval of 10–500 s after the GBM trigger time T_0, which contains all the γ rays detected by the LAT before the GRB exited its FOV. We also select the events with energies between 100 MeV and 10 GeV, and with a zenith angle <100° to limit the contribution from the bright Earth limb. The GRB photon spectrum is modelled with a power law $\mathrm{dN/dE} = AE^{\Gamma}$. The main background component consists of charged particles that are mis-classified as γ rays. It is included in the analysis using the `iso_P8R2_TRANSIENT020_V6_v06.txt` template. Although the contribution from the Galactic diffuse emissions is very small because of the high Galactic latitude of the GRB, it is accounted for by using the `gll_iem_v07.fits` template. Both templates are available at the Fermi Science Support Center (https://fermi.gsfc.nasa.gov/ssc/). No source from the fourth LAT GRB catalogue (4FGL) is bright enough to be considered in the model of the ROI.

To localize the GRB and estimate its signal significance in the LAT, we perform a likelihood ratio test for the presence of the source at different positions[31]. Using the `gttsmap` tool, we evaluate TS to be twice the increment of the logarithm of the likelihood by fitting the data with and without the GRB component added to the background components in the model. The maximum value, $\mathrm{TS_{max}} = 29$, is found at a location of RA = 11.13°, dec. = −24.97° (J2000), consistent with what was first reported by Omodei et al.[32]. This $\mathrm{TS_{max}}$ value corresponds to a detection significance of 4.4σ or 5.0σ (one-sided) if the TS distribution follows $(1/2)\chi^2_4$ or $(1/2)\chi^2_2$, respectively. As explained in the first LAT GRB catalogue[33], the two coordinates of the source are considered to be unknown and are left free to vary in the former case (namely, 4 degrees of freedom including the two spectral parameters), while the latter case is more suitable when an external position is used as an input to the analysis (for example, the GBM initial position here).

We compute the error contours of the source localization from the variation of the TS values around the best position, namely $\mathrm{TS_{max}}$. In each pixel i of the map displayed in Fig. 1, we first compute the difference in TS as $\Delta\mathrm{TS}_i = \mathrm{TS_{max}} - \mathrm{TS}_i$. Then, we convert it to a probability contour level assuming that the $\Delta\mathrm{TS}_i$ is distributed as a χ^2 with 2 degrees of freedom (the two coordinates)[31,33]:

$$p_i = \int_0^{\Delta \mathrm{TS}_i} \chi^2_2(t)\ \mathrm{d}t. \tag{1}$$

The iso-contours containing localization probabilities of 68% and 90% are highlighted in Fig. 1. The best-fit spectral parameters obtained at the position of $\mathrm{TS_{max}}$ are summarized in Extended Data Fig. 1. We also calculate the isotropic energy (E_{iso}) and luminosity (L_{iso}) assuming the distance of the Sculptor galaxy to be about 3.5 megaparsecs[5]. Finally, we use the `gtsrcprob` tool to compute the probability for each LAT γ ray to be associated with the LAT-detected source. The first γ ray exceeding a probability of 90% arrives at $T_0 + 19.18$ s, with an energy of 480 MeV. A 1.3-GeV photon is detected at $T_0 + 180.22$ s, while the highest-energy γ ray is a 1.7-GeV photon at $T_0 + 284.05$ s. All of these γ rays belong to the `SOURCE` class (or to a cleaner event class), which results from a tight event classification that drastically reduces the residual background rate. Extended Data Fig. 2 shows all the γ rays detected within the 12° ROI with their probability of being associated with the GRB. The three γ rays with the highest association probability (>90%) are displayed in Fig. 1 with circles of radius equal to the 68% containment radius of the LAT PSF[34,35].

Spatial association of the high-energy emission with the Sculptor galaxy. Four galaxies from the NGC2000 catalogue[8] (IC 1576, IC 1578, IC 1582 and NGC 253) are located within the ROI centred at the position of the LAT source with radius r_{99}, and many more fainter galaxies are certainly located inside the region. Adding more galaxies from catalogues with a greater limiting magnitude (more fainter galaxies) would vastly increase the number of counterpart candidates. To take this consideration into account, we adopt the LR method[11], applied in several studies for counterpart searches in different catalogues[36–44]. This approach allows us to obtain and quantify the reliability of a possible γ-ray association, using the counterparts' local surface density: in this sense the LR can be used to calculate the probability that a suggested association is the true counterpart of a source. If we define $r_{\alpha,\beta}$ as the angular distance d between the γ-ray localization α and the counterpart candidate β, scaled by the γ-ray location uncertainty (at the 68% confidence level) r_{68}, then it is given by

$$r_{\alpha,\beta} = \frac{d}{r_{68}}. \tag{2}$$

The probability that a counterpart β lies at a distance $r_{\alpha,\beta}$ from the γ-ray localization α is distributed as a Rayleigh distribution ($r_{\alpha,\beta}\ \mathrm{e}^{-r^2_{\alpha,\beta}/2}$), while the probability that β is a background source that, by chance, happens to lie close to the position α follows a linear distribution ($\propto r_{\alpha,\beta}$). The LR can thus be computed as:

$$\mathrm{LR} = \frac{p}{N(\leq m_\beta)A}, \tag{3}$$

where $p = \mathrm{e}^{-r^2_{\alpha,\beta}/2}$, $N(\leq m_\beta)$ is the surface density of sources brighter than the counterpart candidate β (of magnitude m_β) and A is the solid angle spanned by r_{99}. To evaluate the surface density $N(\leq m_\beta)$, we count the galaxies brighter than the candidate β in a region of 20° around the γ-ray source. At the position of the LAT-detected source, the values of the LR for the four galaxies are LR = 2.1 (IC 1576), 2.9 (IC 1578), 0.3 (IC 1582), and 60 (NGC 253). Although two NGC galaxies (IC 1576 and IC 1578) are closer to the LAT best position, the LR favours the most luminous NGC 253 (the Sculptor galaxy). To take into account the extension of the counterpart galaxy, expressed by its radial angular extent in optical r_{ext}, we modified equation (3) for the LR by adding in quadrature r_{ext} to r_{68}. We can write the new equation for LR in a convenient form as:

$$\mathrm{LR_{ext}} = \frac{p^{\xi}}{N(\leq m_\beta)A}, \tag{4}$$

where the exponent ξ is simply defined as:

$$\xi = \frac{1}{1 + \left(\frac{r_{\mathrm{ext}}}{r_{68}}\right)^2}. \tag{5}$$

To quantify the significance of the LR and $\mathrm{LR_{ext}}$ values we perform a set of 10^5 simulations by randomizing the position over the sky of the LAT excess, and repeating the procedure described above. For every random position we select the maximum of the LR and $\mathrm{LR_{ext}}$, which corresponds to the galaxy with greatest association probability within the ROI, and we fill a histogram with these values. The LR method can also be applied using the probability map illustrated in Fig. 1. From this map we can directly evaluate $1 - p_i$, with p_i from equation (1), and use it as the numerator in the LR formula. In this way, we consider the shape of the TS map and we abandon the hypothesis implicit in the Rayleigh distribution that the two spatial coordinates are are independently normally distributed. As in the previous case, we generate 10^5 observations, choosing the position of the TS map randomly on the celestial sphere. For each location, we compute the LR values for the NGC galaxies in the ROI, considering them as point-like or extended sources. The P values quantify the potential association between the Sculptor galaxy and the LAT γ-ray source. They are defined as the number of cases where the LR is greater than that obtained for the Sculptor galaxy divided by the total number of simulated cases. They can thus be obtained from the normalized cumulative distributions, displayed in Extended Data Fig. 3. The two distributions (point-like versus extended source) are similar and yield comparable association probabilities. For the Rayleigh case, P values range from 1.7×10^{-3} to 2.9×10^{-3}, whereas using the TS map to compute the LR gives lower P values, 3.2×10^{-4} for point-like sources and 3.6×10^{-4} for extended sources. Lower P values are expected from this second analysis given the elongation of the TS map toward the Sculptor galaxy, with a smaller value for the extended case because of the large extension of the Sculptor galaxy (around 25 arcmin). Assuming that the emission detected at high energies is from a SGRB, we can calculate the FAR by multiplying the P values by the rate of SGRBs observed by the LAT. Values range from $5.4 \times 10^{-4}\ \mathrm{yr^{-1}}$ to $4.7 \times 10^{-3}\ \mathrm{yr^{-1}}$ as summarized in the first part of Extended Data Fig. 4. Both the analyses suggest a strong likelihood of positional association between the Sculptor galaxy and the LAT γ-ray source.

Significance of the temporal coincidence. From Extended Data Fig. 2, we can see that three γ rays with energies 0.5 GeV, 1.3 GeV and 1.7 GeV are reconstructed within 1° of Sculptor, and they arrive within a time span of approximately 300 s.

We calculate the significance of the LAT triplet by selecting all the SOURCE events (between 100 MeV and 300 GeV) received by the LAT in 12 years of data within a radius of 1° from the centre of the Sculptor galaxy (RA = 11.89°, dec. = −25.29°, J2000). The total live time of the selected ROI is about 2.98 yr. To compute the probability that three photons cluster by chance, owing to statistical fluctuations of the background, in the 10–500 s interval after T_0, we apply the LR method of ref. [12]. The maximum likelihood ratio, testing the presence of a new source, is defined as:

$$\lambda = \left[\frac{\alpha}{1+\alpha}\left(1+\frac{N_B}{N_S}\right)\right]^{N_S}\left[\frac{1}{1+\alpha}\left(1+\frac{N_S}{N_B}\right)\right]^{N_B}, \quad (6)$$

where $N_S = 3$ and $N_B = 5361$ are respectively the number of LAT photons observed during and outside the analysis time window and α is the ratio between the analysed time interval (490 s) and the total live time (about 2.98 yr). The significance S of the LAT triplet signal can thus be calculated as:

$$S \approx \sqrt{-2\ln\lambda} = 5.3\sigma, \quad (7)$$

corresponding to a P value of 8.3×10^{-7}. To estimate whether such a cluster of three events is common for the analysed ROI, we use again the entire LAT dataset of the Sculptor galaxy region to compute the time intervals Δt_i for each triplet i formed by three consecutive events:

$$\Delta t_i = t_{i+2} - t_i. \quad (8)$$

Thus, the resulting intervals are used to create the dashed red histogram of Extended Data Fig. 5, in which the blue line corresponds to the Fermi orbit period and the yellow line shows the Δt of the triplet of photons observed for the LAT-detected source. This simple analysis does not consider that the ROI periodically enters and exits the LAT FOV, potentially splitting some triplets into different time windows. To take this effect into account, we perform a second and more conservative analysis subtracting from each Δt_i the duration of the time intervals during which the ROI is not observable (bad time intervals). As expected, the bulk of the distribution moves toward shorter time intervals (green histogram in Extended Data Fig. 5) but no significant new entries appear at the tail of the distribution. This corrected histogram is in agreement with the theoretical curve expected in the case of independent events (black dashed line in Extended Data Fig. 5). For a Poisson distribution of γ ray arrival times from a steady source, indeed, the probability density P of observing a triplet with time interval Δt given the mean rate R is:

$$P(\Delta t) = R^2\Delta t\ \mathrm{e}^{-R\Delta t}. \quad (9)$$

with a rate $R \approx 5.7\times10^{-5}$ Hz, this results in a probability of 1.4×10^{-4} for an interval shorter than $\Delta t \approx 300$ s.

We find that three events clustered in a time window shorter than the one related to the LAT source on only one occasion over 12 years (within an interval of 240 s starting at 2017 November 21 at 03:07:33 UTC), but the likelihood analysis of this triplet resulted in a low detection significance ($TS_{max} = 16$).

We compute the FAR (in units of hertz) for the temporal coincidence of the LAT-detected source with GRB 200415A as:

$$\mathrm{FAR} = A\times\ R_{\mathrm{triplet}}\times R_{\mathrm{GRB}}\times\delta t \quad (10)$$

where $A = \pi$ deg² is the area of the circular region under consideration, $R_{GRB} = 3.7\times10^{-11}$ s^{-1} deg^{-2} is the rate of SGRBs detected by the GBM, obtained from the online catalogue of GBM GRBs[45] and scaled by the GBM FOV, and $\delta t = 500$ s is the coincidence time window after the SGRB prompt emission during which we expect a signal in the LAT data. $R_{triplet}$ is the mean rate of triplets having a Δt smaller than a fixed threshold and, for a value of 500 s, we count only eight triplets over 2.98 yr of live time (see Extended Data Fig. 5). The resulting FAR is 1.6×10^{-7} yr^{-1}. Considering only events with energies greater than 480 MeV (the energy of the least-energetic photon within the cluster associated with the GRB), we find only the triplet related to the MGF and the FAR accordingly decreases to 2×10^{-8} yr^{-1}.

We also apply the Bayesian blocks (BB) algorithm[13,14] to the dataset with the bad time intervals removed. We used BB to detect and characterize statistically significant variations in rates of LAT γ rays, such as the photon time tags analysed here. It provides optimal, maximum goodness of fit, segmentation of the observed time series, from among all possible partitions of the observation interval. The arrival times of the photons are binned using the BB edges, and a rate for each block is obtained by dividing its number of included photons by its width in time. The only free parameter describes the prior for the distribution of the number of blocks. Within a range suggested by calibrations based on limiting the false positive rate for single change-point detection[14], this penalty constant can be adjusted in the same spirit as with a smoothing parameter. Extended Data Fig. 6 shows the results of this analysis for a selected value of the penalty constant, together with daily and weekly count rates. We also display the weekly average exposures. Three epochs are shaded in yellow, corresponding to three distinct observing profiles. The first, at the beginning of the mission, coincides with the period in which Fermi had a 35° rocking angle. This represents the angle between the zenith and the pointing direction of the LAT and was gradually increased until it reached 55° in September 2009. Between December 2013 and July 2015, instead, Fermi spent most of its time pointing at the Galactic Centre: this corresponds to the second highlighted interval, which is consequently characterized, on average, by a decrease of exposure in the direction of the Sculptor galaxy. The third highlighted period starts with the occurrence of the solar panel drive anomaly of the Fermi spacecraft (https://fermi.gsfc.nasa.gov/ssc/observations/types/post_anomaly/), in March 2018 and ends when a new optimized observing profile was adopted to mitigate the effect of this issue in February 2019. Spikes and dips in the exposure are the effect of occasional pointed observations (called targets of opportunity). However, at the time of GRB 200415A no particular features are evident in the time dependence of the accumulation of exposure. The clear spike of γ-ray rate at T_0 corresponds to the cluster of the events arriving within about 300 s. In particular, there are three events in the bin with the highest rate (and a width of 810 s). From simple Poisson statistics, considering the average rate of γ rays detected from the direction of Sculptor in the remaining time history, the probability of this rate being a fluctuation is 2.3×10^{-3}.

Finally, to estimate the FAR we use a formula similar to equation (10), with $\delta t = 810$ s (the width of the time block) and $R_{triplet}$ replaced by R_{block}, namely, the average detection rate of blocks exceeding a threshold of 10^{-3} Hz. With just two such blocks in 2.98 yr of total live time (see Extended Data Fig. 6), the corresponding FAR is 6.3×10^{-8} yr^{-1}. These results are summarized in the second part of Extended Data Fig. 4.

Comparison with other LAT SGRBs. Here we compare GRB 200415A with the population of GRBs detected by the LAT. The spectrum of GRB 200415A is typical for short bursts detected by the LAT, with a photon index $\Gamma = -1.7\pm0.3$ consistent with the distribution of photon indices $\Gamma_{ext} = -2.03\pm-0.4$ (at 90% confidence level) of the 2FLGC. In that catalogue, the subscript 'ext' indicates that the integration window that is used to compute the photon index is restricted to the duration of the temporally extended emission detected by the LAT, which is the most appropriate in the comparison with the photon index of GRB 200415A. The flux and fluence measured for GRB 200415A are also typical, being on the low end of the distributions. What is quite peculiar about the LAT emission from GRB 200415A is its delay and duration.

The left-hand panel of Extended Data Fig. 7, from the 2FLGC, shows the arrival time of the first LAT γ ray with probability >0.9 of association with the GRB, which marks the beginning of the high-energy emission, as a function of the GBM T_{95}, which marks the end of the prompt emission observed by the GBM[4]. For a short burst, GRB 200415A has a exceptionally delayed high-energy emission with respect to the end of the prompt phase. Two other short bursts in the 2FLGC show comparable delays: GRB 160702A was detected by Konus-Wind, INTEGRAL (SPI-ACS), Mars-Odyssey (HEND), and Swift (BAT)[46]. Fermi was in the South Atlantic Anomaly at the time of the trigger, precluding a search for high-energy emission during (or immediately after) the prompt emission. Similarly, GRB 170127 was outside the FOV of the LAT, with a boresight angle of 142° at the time of the GBM trigger. An autonomous re-pointing request was issued by the GBM, and the LAT detected high-energy emission once the burst entered its FOV. GRB 200415A is the only LAT SGRB that was within the FOV at the time of trigger, and additionally its high-energy emission started much later than the end of the GBM prompt emission. The right-hand panel of Extended Data Fig. 7 shows that GRB 200415A has a relatively long duration at high energies for a SGRB. Again, only the same two other SGRBs mentioned above have similar durations.

GeV γ-ray flare from ultra-relativistic debris from a magnetar colliding with an outlying shell. An MGF is a catastrophic event in the life-cycle of a magnetar, releasing a sizeable fraction of its approximately 10^{48} erg magnetic energy[16,47]. Different trigger mechanisms have been proposed for an MGF, for example, a rupture of the solid crust due to magnetic stress at the core–cusp boundary[16], or a deformation of the magnetosphere[17,18]. Such a process releases a huge amount of energy within a very short period of time in a small volume near the magnetar with radius $r_0 = 10^6 r_{0,6}$ cm. This produces copious $e^{\pm}$ pairs and an optically thick fireball[48,49]. A qualitative description of this fireball and its evolution[19,20] depends on its total luminosity $L_0 = L_{\gamma,\mathrm{iso}}/\xi_\gamma \approx 3\times10^{47}\,\xi_{\gamma,-0.5}^{-1}L_{\gamma,47}$ erg s^{-1}. Here $L_{\gamma,\mathrm{iso}} = 10^{47}L_{\gamma,47}$ erg s^{-1} is the average isotropic-equivalent γ-ray luminosity during the prompt duration containing 90% of the fluence $T_{90} = 0.141$ s period[4], and $\xi_\gamma = 0.3\xi_{\gamma,-0.5}$ is the assumed fraction of the total luminosity in γ rays, which includes the magnetic energy and kinetic energy carried by the baryons in the fireball. The initial effective temperature of the fireball is $T_0 = (L_0/4\pi r_0^2 ca)^{1/4} \approx 275\ \xi_{\gamma,-0.5}^{-1/4}L_{\gamma,47}^{1/4}r_{0,6}^{-1/2}$ keV; note that the luminosity is lower than that indicative of full thermalization[4]. Here $a = \pi^2k^4/15\hbar^3c^3 = 7.6\times10^{-15}$ erg cm^{-3} K^{-4} is the radiation density constant. A key finding for GRB 200415A is that the total energy in the LAT emission, $E_{\mathrm{LAT,iso}} = 3.6\times10^{45}$ erg, is much less than the prompt GBM energy of 1.5×10^{46} erg[4]. This implies that the fireball is ultra-relativistic and the kinetic outflow attains a terminal bulk Lorentz factor similar to a critical value obtained from the Thomson opacity argument as[19,20] $\eta_* = (L_0\sigma_T/4\pi m_p c^3 r_0)^{1/4} \approx 140\ \xi_{\gamma,-0.5}^{-1/4}L_{\gamma,47}^{1/4}r_{0,6}^{-1/4}$. Here

σ_T is the Thomson cross-section and m_p is the mass of the proton. The total isotropic-equivalent energy of the kinetic outflow (ejecta), after decoupling from the radiation, is $E_{k,iso}=3\times10^{46}E_{k,46.5}$ erg with a bulk Lorentz factor $\Gamma_{ej}=10^2\Gamma_{ej,2}$, where the parameters $E_{k,46.5}\approx\Gamma_{ej,2}\approx1$. These numbers may change somewhat if the influence of field line flaring in modifying the outflow dynamics is fully taken into account. As we discuss next and in contrast to the previously modelled radio nebula from the 2004 MGF of SGR 1806-20 with an outflow velocity of about $0.7c$ (refs. [21,22]),this ultra-relativistic kinetic outflow is critical for our interpretation of the LAT observation.

Absent an intermediate electron acceleration site, for example a magnetic reconnection zone in the MHD wind outside the light cylinder, no relevant emission is produced from the outflow before it interacts with an external shell. The external shell is naturally produced as the spindown-powered relativistic pulsar-type MHD wind emanating from the magnetar sweeps up the surrounding interstellar medium (ISM) and creates a bow shock. The radial distance of the shell is found from balancing in the rest frame of the magnetar (and of the head of the bow shock) the ram pressure of the incoming ISM with that of the MHD wind. For nominal values of the spin-down luminosity $L_{sd}=10^{34}L_{sd,34}\,\mathrm{erg\,s^{-1}}$, the proper motion velocity of the magnetar $v=10^3v_3\,\mathrm{km\,s^{-1}}$ and the ISM density $n=10^{-1.6}n_{-1.6}\,\mathrm{cm^{-3}}$, the radius of the bow shock is $R_{bs}=(L_{sd}/4\pi nm_pv^2c)^{1/2}=8\times10^{15}L_{sd,34}^{1/2}n_{-1.6}^{-1/2}v_3^{-1}$ cm . The bow-shock shell has an inner part of shocked MHD wind and an outer part of shocked ISM, the two being separated by a contact discontinuity.

The observed collision time between the outflow, which propagates essentially in vacuum, and the bow-shock shell is given by $t_{coll}=R_{bs}/2\Gamma_{ej}^2c\approx10$ s, where we identify t_{coll} with the arrival time of the first photons to the observer from the head of the outflow along the line of sight. The duration of LAT emission, however, depends on the angular time scale over which emission arrives from the shocked outflow and bow-shock shell. This time scale is $t_\theta=R_{bs}/2\Gamma_{sh}^2c$, where Γ_{sh} is the bulk Lorentz factor of the forward shock propagating in the outer part of the shell with shocked ISM (the inner part with shocked wind offers negligible resistance). For a strong shock the density contrast between the outflow and bow-shock shell is $f\equiv n_{ej}/n_{bs}\approx30\ L_{sd,34}^{-3/2}E_{k,46.5}n_{-1.6}^{1/2}v_3^3$, after calculating the outflow ejecta density $n_{ej}=E_{k,iso}/4\pi R_{bs}^3m_pc^2\approx3\ L_{sd,34}^{-3/2}E_{k,46.5}n_{-1.6}^{3/2}v_3^3\ \mathrm{cm^{-3}}$ and $n_{bs}\approx4n\approx0.1n_{-1.6}\,\mathrm{cm^{-3}}$. As a result[50], $\Gamma_{sh}=f^{1/4}(\Gamma_{ej}/2)^{1/2}\approx20\ L_{sd,34}^{-1/4}t_{coll,1}^{-1/4}E_{k,46.5}^{1/4}v_3^{1/2}$ and $t_\theta\approx400\ L_{sd,34}t_{coll,1}^{1/2}E_{k,46.5}^{-1/2}n_{-1.6}^{-1/2}v_3^{-2}$s is sufficiently long to account for the duration of the LAT emission of about 300 s.

The LAT emission is produced by the shock-accelerated electrons in the material behind the forward shock that is propagating into the bow shock. The radiation efficiency $E_{LAT,iso}/E_{k,iso}\approx0.1$ is typical of GRB afterglow emission. The maximum synchrotron photon energy emitted by these electrons is limited by their acceleration and cooling times to[51] $E_{syn,max}=\Gamma_{sh}\kappa(m_ec^2/\alpha_F)\approx1.4\kappa L_{sd,34}^{-1/4}t_{coll,1}^{-1/4}E_{k,46.5}^{1/4}v_3^{1/2}$ GeV, where $\alpha_F=e^2/\hbar c\approx1/137$ is the fine-structure constant. The factor κ is of order unity[52] and can be different for differing assumptions about electron acceleration rates and diffusion in a shock layer. Therefore, the synchrotron photon energy can explain the highest-energy LAT γ ray observed from GRB 200415A if $\Gamma_{sh}\gtrsim20$.

Data availability

The Fermi-LAT data are publicly available at the Fermi Science Support Center website: https://fermi.gsfc.nasa.gov/ssc/. Filtered data supporting the findings of this study are available at https://www-glast.stanford.edu/pub_data/1801/.

Code availability

In this study we use the Fermi-LAT Science Tools, publicly available at the Fermi Science Support Center website: https://fermi.gsfc.nasa.gov/ssc/. The code required to reproduce each figure of the paper is available from the corresponding authors upon request.

Received: 20 October 2020; Accepted: 1 December 2020;
Published online: 13 January 2021

References

1. Frail, D. A., Kulkarni, S. R. & Bloom, J. S. An outburst of relativistic particles from the soft γ-ray repeater SGR1900+14. *Nature* **398**, 127–129 (1999).
2. Hurley, K. et al. An exceptionally bright flare from SGR 1806-20 and the origins of short-duration γ-ray bursts. *Nature* **434**, 1098–1103 (2005).
3. Svinkin, D. & the IPN Team. Bright twin γ-ray flares in two nearby galaxies as giant magnetar flares. *Nature* https://doi.org/10.1038/s41586-020-03076-9 (2021).
4. Roberts, O. J. & the GBM and Swift Teams. Rapid spectral variability of a giant flare from an extragalactic magnetar. *Nature* https://doi.org/10.1038/s41586-020-03077-8 (2021).
5. Rekola, R. et al. Distance to NGC 253 based on the planetary nebula luminosity function. *Mon. Not. R. Astron. Soc.* **361**, 330–336 (2005).
6. Frederiks, D. D. et al. On the possibility of identifying the short hard burst GRB 051103 with a giant flare from a soft gamma repeater in the M81 group of galaxies. *Astron. Lett.* **33**, 19–24 (2007).
7. Mazets, E. P. et al. A giant flare from a soft gamma repeater in the Andromeda galaxy (M31). *Astrophys. J.* **680**, 545–549 (2008).
8. *VizieR Online Data Catalog* NGC 2000.0 VII/118 (Sky Publishing, 1988); http://go.nature.com/3bsaO6o
9. Abdollahi, S. et al. Fermi Large Area Telescope fourth source catalog. *Astrophys. J. Suppl.* **247**, 33 (2020).
10. Ackermann, M. et al. GeV observations of star-forming galaxies with the Fermi Large Area Telescope. *Astrophys. J.* **755**, 164 (2012).
11. de Ruiter, H. R., Willis, A. G. & Arp, H. C. A Westerbork 1415 MHz survey of background radio sources. II. Optical identifications with deep IIIa-J plates. *Astron. Astrophys. Suppl.* **28**, 211–293 (1977).
12. Li, T. P. & Ma, Y. Q. Analysis methods for results in gamma-ray astronomy. *Astrophys. J.* **272**, 317–324 (1983).
13. Scargle, J. D. Studies in astronomical time series analysis. V. Bayesian blocks, a new method to analyze structure in photon counting data. *Astrophys. J.* **504**, 405 (1998).
14. Scargle, J. D., Norris, J. P., Jackson, B. & Chiang, J. Studies in astronomical time series analysis. VI. Bayesian block representations. *Astrophys. J.* **764**, 167 (2013).
15. Story, S. A. & Baring, M. G. Magnetic pair creation transparency in gamma-ray pulsars. *Astrophys. J.* **790**, 61 (2014).
16. Thompson, C. & Duncan, R. C. The soft gamma repeaters as very strongly magnetized neutron stars—I. Radiative mechanism for outbursts. *Mon. Not. R. Astron. Soc.* **275**, 255–300 (1995).
17. Lyutikov, M. Mass-loading of pulsar winds. *Mon. Not. R. Astron. Soc.* **339**, 623–632 (2003).
18. Gill, R. & Heyl, J. S. On the trigger mechanisms for soft gamma-ray repeater giant flares. *Mon. Not. R. Astron. Soc.* **407**, 1926–1932 (2010).
19. Ioka, K., Razzaque, S., Kobayashi, S. & Mészáros, P. TeV-PeV neutrinos from giant flares of magnetars and the case of SGR 1806-20. *Astrophys. J.* **633**, 1013–1017 (2005).
20. Nakar, E., Piran, T. & Sari, R. Pure and loaded fireballs in soft gamma-ray repeater giant flares. *Astrophys. J.* **635**, 516–521 (2005).
21. Gelfand, J. D. et al. A rebrightening of the radio nebula associated with the 2004 December 27 giant flare from SGR 1806-20. *Astrophys. J. Lett.* **634**, L89–L92 (2005).
22. Granot, J. et al. Diagnosing the outflow from the SGR 1806-20 giant flare with radio observations. *Astrophys. J.* **638**, 391–396 (2006).
23. Cheng, K. S. & Wang, X. Y. The radio afterglow from the giant flare of SGR 1900+14: the same mechanism as afterglows from classic gamma-ray bursts? *Astrophys. J. Lett.* **593**, L85–L88 (2003).
24. Hurley, K. The short gamma-ray burst—SGR giant flare connection. *Adv. Space Res.* **47**, 1337–1340 (2011).
25. Abdo, A. A. et al. Search for gamma-ray emission from magnetars with the Fermi Large Area Telescope. *Astrophys. J. Lett.* **725**, L73–L78 (2010).
26. Li, J., Rea, N., Torres, D. F. & de Oña-Wilhelmi, E. Gamma-ray upper limits on magnetars with six years of Fermi-LAT observations. *Astrophys. J.* **835**, 30 (2017).
27. Ajello, M. et al. A decade of gamma-ray bursts observed by Fermi-LAT: the second GRB catalog. *Astrophys. J.* **878**, 52 (2019).
28. Atwood, W. B. et al. The Large Area Telescope on the Fermi Gamma-Ray Space Telescope Mission. *Astrophys. J.* **697**, 1071–1102 (2009).
29. Meegan, C. et al. The Fermi Gamma-ray Burst Monitor. *Astrophys. J.* **702**, 791 (2009).
30. Bissaldi, E. et al. GRB 200415A: Fermi GBM observation. *GRB Coord. Netw.* No. 27587 (2020).
31. Mattox, J. R. et al. The likelihood analysis of EGRET data. *Astrophys. J.* **461**, 396 (1996).
32. Omodei, N. et al. GRB 200415A: Fermi-LAT localization update. *GRB Coord. Netw.* No. 27597 (2020).
33. Ackermann, M. et al. The first Fermi-LAT gamma-ray burst catalog. *Astrophys. J. Suppl.* **209**, 11 (2013).
34. Abdo, A. A. et al. The on-orbit calibration of the Fermi Large Area Telescope. *Astropart. Phys.* **32**, 193–219 (2009).
35. Atwood, W. et al. Pass 8: toward the full realization of the Fermi-LAT scientific potential. Preprint at https://arxiv.org/abs/1303.3514 (2013).
36. Sutherland, W. & Saunders, W. On the likelihood ratio for source identification. *Mon. Not. R. Astron. Soc.* **259**, 413–420 (1992).
37. Masci, F. J. et al. A new complete sample of submillijansky radio sources: an optical and near-infrared study. *Publ. Astron. Soc. Pac.* **113**, 10–28 (2001).
38. Ciliegi, P. et al. A deep VLA survey at 6 cm in the Lockman Hole. *Astron. Astrophys.* **398**, 901–918 (2003).
39. Ackermann, M. et al. The second catalog of active galactic nuclei detected by the Fermi Large Area Telescope. *Astrophys. J.* **743**, 171 (2011).
40. Ackermann, M. et al. The first Fermi-LAT catalog of sources above 10 GeV. *Astrophys. J. Suppl.* **209**, 34 (2013).

41. McAlpine, K., Jarvis, M. J. & Bonfield, D. G. Evolution of faint radio sources in the VIDEO-XMM3 field. *Mon. Not. R. Astron. Soc.* **436**, 1084–1095 (2013).
42. Ackermann, M. et al. The third catalog of active galactic nuclei detected by the Fermi Large Area Telescope. *Astrophys. J.* **810**, 14 (2015).
43. Ajello, M. et al. The fourth catalog of active galactic nuclei detected by the Fermi Large Area Telescope. *Astrophys. J.* **892**, 105 (2020).
44. de Menezes, R., D'Abrusco, R., Massaro, F., Gasparrini, D. & Nemmen, R. On the physical association of Fermi-LAT blazars with their low-energy counterparts. *Astrophys. J. Suppl.* **248**, 23 (2020).
45. von Kienlin, A. et al. The fourth Fermi-GBM gamma-ray burst catalog: a decade of data. *Astrophys. J.* **893**, 46 (2020).
46. Hurley, K. et al. IPN triangulation of GRB 160702A (short/hard). *GRB Coord. Netw.* No. 19666 (2016).
47. Kaspi, V. M. & Beloborodov, A. M. Magnetars. *Annu. Rev. Astron. Astrophys.* **55**, 261–301 (2017).
48. Paczynski, B. Gamma-ray bursters at cosmological distances. *Astrophys. J. Lett.* **308**, L43–L46 (1986).
49. Goodman, J. Are gamma-ray bursts optically thick? *Astrophys. J. Lett.* **308**, L47 (1986).
50. Sari, R. & Piran, T. Hydrodynamic timescales and temporal structure of gamma-ray bursts. *Astrophys. J. Lett.* **455**, 143 (1995).
51. Razzaque, S., Dermer, C. D. & Finke, J. D. Synchrotron radiation from ultra-high energy protons and the Fermi observations of GRB 080916C. *Open Astron. J.* **3**, 150–155 (2010).
52. De Jager, O. et al. Gamma-ray observations of the Crab nebula: a study of the synchro-compton spectrum. *Astrophys. J.* **457**, 253 (1996).

Acknowledgements

The Fermi-LAT Collaboration acknowledges support for LAT development, operation and data analysis from NASA and the Department of Energy (United States), CEA/Irfu and IN2P3/CNRS (France), ASI and INFN (Italy), MEXT, KEK and JAXA (Japan), and the K. A. Wallenberg Foundation, the Swedish Research Council and the National Space Board (Sweden). Science analysis support in the operations phase from INAF (Italy) and CNES (France) is also gratefully acknowledged. This work was performed in part under Department of Energy contract DE-AC02-76SF00515. E. Burns is a NASA Postdoctoral Program Fellow.

Author contributions

The Fermi-LAT was designed and constructed by the Fermi-LAT Collaboration. The operation, data processing, calibration, Monte Carlo simulations of the detector and of theoretical models, and data analyses were performed by the members of the Fermi-LAT Collaboration. All Fermi-LAT collaborators that signed this paper contributed to the editing of and comments on the final version of the manuscript. A.B., N. Di Lalla, N.O. and F.P. contributed to the analysis and the writing of the manuscript and S. Razzaque provided the interpretation and contributed to the writing of the paper.

Competing interests

The authors declare no competing financial interests.

Additional information

Extended data is available for this paper at https://doi.org/10.1038/s41550-020-01287-8.

Correspondence and requests for materials should be addressed to A.B., N.D.L., N.O., F.P. or S.R.

Peer review information *Nature Astronomy* thanks the anonymous reviewers for their contribution to the peer review of this work.

Reprints and permissions information is available at www.nature.com/reprints.

Publisher's note Springer Nature remains neutral with regard to jurisdictional claims in published maps and institutional affiliations.

The Fermi-LAT Collaboration

M. Ajello[1], W. B. Atwood[2], M. Axelsson[3,4], L. Baldini[5], G. Barbiellini[6,7], M. G. Baring[8], D. Bastieri[9,10], R. Bellazzini[11], A. Berretta[12] ✉, E. Bissaldi[13,14], R. D. Blandford[15], R. Bonino[16,17], J. Bregeon[18], P. Bruel[19], R. Buehler[20], E. Burns[21,22], S. Buson[23], R. A. Cameron[15], P. A. Caraveo[24], E. Cavazzuti[25], S. Chen[9,26], C. C. Cheung[27], G. Chiaro[24], S. Ciprini[28,29], D. Costantin[30], M. Crnogorcevic[31], S. Cutini[32], F. D'Ammando[33], P. de la Torre Luque[13], F. de Palma[16], S. W. Digel[15], N. Di Lalla[15] ✉, L. Di Venere[13,14], F. Fana Dirirsa[34], Y. Fukazawa[35], S. Funk[36], P. Fusco[13,14], F. Gargano[14], N. Giglietto[13,14], R. Gill[37,38], F. Giordano[13,14], M. Giroletti[33], J. Granot[38], D. Green[39], I. A. Grenier[40], S. Griffin[22], S. Guiriec[22,37], E. Hays[22], D. Horan[19], G. Jóhannesson[41,42], M. Kerr[27], M. Kovačević[32], M. Kuss[11], S. Larsson[4,43,44], L. Latronico[16], J. Li[20], F. Longo[6,7], F. Loparco[13,14], M. N. Lovellette[27], P. Lubrano[32], S. Maldera[16], A. Manfreda[5], G. Martí-Devesa[45], M. N. Mazziotta[14], J. E. McEnery[22,31], I. Mereu[12,32], P. F. Michelson[15], T. Mizuno[46], M. E. Monzani[15], A. Morselli[28], I. V. Moskalenko[15], M. Negro[47,48], N. Omodei[15] ✉, M. Orienti[33], E. Orlando[15,49], V. S. Paliya[20], D. Paneque[39], Z. Pei[10], M. Pesce-Rollins[11], F. Piron[18] ✉, H. Poon[35], T. A. Porter[15], G. Principe[33], J. L. Racusin[22], S. Rainò[13,14], R. Rando[9,26,50], B. Rani[22,51], S. Razzaque[52] ✉, A. Reimer[15,45], O. Reimer[45], P. M. Saz Parkinson[2,53,54], J. D. Scargle[55], L. Scotton[18], D. Serini[13], C. Sgrò[11], E. J. Siskind[56], G. Spandre[11], P. Spinelli[13,14], H. Tajima[15,57], M. N. Takahashi[39], D. Tak[22,58], D. F. Torres[59,60], G. Tosti[12,32], E. Troja[22,31], Z. Wadiasingh[22], K. Wood[61], M. Yassine[6,7], A. Yusafzai[36] and G. Zaharijas[49,62]

[1]Department of Physics and Astronomy, Clemson University, Kinard Lab of Physics, Clemson, SC, USA. [2]Santa Cruz Institute for Particle Physics, Department of Physics and Department of Astronomy and Astrophysics, University of California at Santa Cruz, Santa Cruz, CA, USA. [3]Department of Physics, Stockholm University, Stockholm, Sweden. [4]Department of Physics, KTH Royal Institute of Technology, Stockholm, Sweden. [5]Università di Pisa and Istituto Nazionale di Fisica Nucleare, Pisa, Italy. [6]Istituto Nazionale di Fisica Nucleare, Trieste, Italy. [7]Dipartimento di Fisica, Università di Trieste, Trieste, Italy. [8]Department of Physics and Astronomy, Rice University, Houston, TX, USA. [9]Istituto Nazionale di Fisica Nucleare, Padua, Italy. [10]Dipartimento di Fisica e Astronomia "Galileo Galilei", Università di Padova, Padua, Italy. [11]Istituto Nazionale di Fisica Nucleare, Pisa, Italy. [12]Dipartimento di Fisica, Università degli Studi di Perugia, Perugia, Italy. [13]Dipartimento di Fisica, "M. Merlin" dell'Università e del Politecnico di Bari, Bari, Italy.

[14]Istituto Nazionale di Fisica Nucleare, Bari, Italy. [15]W. W. Hansen Experimental Physics Laboratory, Kavli Institute for Particle Astrophysics and Cosmology, Department of Physics and SLAC National Accelerator Laboratory, Stanford University, Stanford, CA, USA. [16]Istituto Nazionale di Fisica Nucleare, Turin, Italy. [17]Dipartimento di Fisica, Università degli Studi di Torino, Turin, Italy. [18]Laboratoire Univers et Particules de Montpellier, Université Montpellier, CNRS/IN2P3, Montpellier, France. [19]Laboratoire Leprince-Ringuet, École polytechnique, CNRS/IN2P3, Palaiseau, France. [20]Deutsches Elektronen Synchrotron (DESY), Zeuthen, Germany. [21]Department of Physics and Astronomy, Louisiana State University, Baton Rouge, LA, USA. [22]NASA Goddard Space Flight Center, Greenbelt, MD, USA. [23]Institut für Theoretische Physik and Astrophysik, Universität Würzburg, Würzburg, Germany. [24]INAF-Istituto di Astrofisica Spaziale e Fisica Cosmica Milano, Milan, Italy. [25]Italian Space Agency, Rome, Italy. [26]Department of Physics and Astronomy, University of Padova, Padua, Italy. [27]Space Science Division, Naval Research Laboratory, Washington, DC, USA. [28]Istituto Nazionale di Fisica Nucleare, Rome, Italy. [29]Space Science Data Center - Agenzia Spaziale Italiana, Rome, Italy. [30]Department of Statistical Science, University of Padua, Padua, Italy. [31]Department of Astronomy, University of Maryland, College Park, MD, USA. [32]Istituto Nazionale di Fisica Nucleare, Perugia, Italy. [33]INAF Istituto di Radioastronomia, Bologna, Italy. [34]Department of Physics, University of Johannesburg, Johannesburg, South Africa. [35]Department of Physical Sciences, Hiroshima University, Hiroshima, Japan. [36]Friedrich-Alexander Universität Erlangen-Nürnberg, Erlangen Centre for Astroparticle Physics, Erlangen, Germany. [37]Department of Physics, The George Washington University, Washington, DC, USA. [38]Department of Natural Sciences, Open University of Israel, Ra'anana, Israel. [39]Max-Planck-Institut für Physik, Munich, Germany. [40]AIM, CEA, CNRS, Université Paris-Saclay, Université Paris Diderot, Gif-sur-Yvette, France. [41]Science Institute, University of Iceland, Reykjavik, Iceland. [42]Nordita, Royal Institute of Technology and Stockholm University, Stockholm, Sweden. [43]The Oskar Klein Centre for Cosmoparticle Physics, Stockholm, Sweden. [44]School of Education, Health and Social Studies, Natural Science, Dalarna University, Falun, Sweden. [45]Institut für Astro- und Teilchenphysik, Leopold-Franzens-Universität Innsbruck, Innsbruck, Austria. [46]Hiroshima Astrophysical Science Center, Hiroshima University, Hiroshima, Japan. [47]Center for Research and Exploration in Space Science and Technology (CRESST) and NASA Goddard Space Flight Center, Greenbelt, MD, USA. [48]Department of Physics and Center for Space Sciences and Technology, University of Maryland, Baltimore, MD, USA. [49]Istituto Nazionale di Fisica Nucleare, and Università di Trieste, Trieste, Italy. [50]Center for Space Studies and Activities "G. Colombo", University of Padova, Padua, Italy. [51]Korea Astronomy and Space Science Institute, Daejeon, Korea. [52]Centre for Astro-Particle Physics (CAPP) and Department of Physics, University of Johannesburg, Johannesburg, South Africa. [53]Department of Physics, The University of Hong Kong, Hong Kong, China. [54]Laboratory for Space Research, The University of Hong Kong, Hong Kong, China. [55]Space Sciences Division, NASA Ames Research Center, Moffett Field, CA, USA. [56]NYCB Real-Time Computing Inc., Lattingtown, NY, USA. [57]Solar-Terrestrial Environment Laboratory, Nagoya University, Nagoya, Japan. [58]Department of Physics, University of Maryland, College Park, MD, USA. [59]Institute of Space Sciences (CSICIEEC), Barcelona, Spain. [60]Institució Catalana de Recerca i Estudis Avançats (ICREA), Barcelona, Spain. [61]Praxis Inc., Alexandria, VA, USA; resident at Naval Research Laboratory, Washington, DC, USA. [62]Center for Astrophysics and Cosmology, University of Nova Gorica, Nova Gorica, Slovenia. ✉e-mail: alessandra.berretta@pg.infn.it; niccolo.dilalla@stanford.edu; nicola.omodei@stanford.edu; piron@in2p3.fr; srazzaque@uj.ac.za

Source	Parameter	Value	Units	T.S.
LAT source	Index (Γ)	-1.7 ± 0.3		29
	Energy Flux	$(4.8 \pm 2.7) \times 10^{-9}$	$\mathrm{erg\,cm^{-2}\,s^{-1}}$	
	Flux	$(4.1 \pm 2.2) \times 10^{-6}$	$\mathrm{cm^{-2}\,s^{-1}}$	
	L_{iso}	$(7.4 \pm 4.2) \times 10^{42}$	$\mathrm{erg\,s^{-1}}$	
	E_{iso}	$(3.6 \pm 2.1) \times 10^{45}$	erg	
GalacticTemplate	Const	1 (fixed)		1
IsotropicTemplate	Const	1.0±0.8		3

Extended Data Fig. 1 | Best-fit parameters from the LAT unbinned likelihood analysis. All fluxes are calculated in the 100 MeV to 10 GeV energy range.

Time since T_0 (s)	Energy (MeV)	R.A. (°)	Dec (°)	Prob.	Dist.$_{NGC253}$ (°)	σ_{68} (°)
19.18	**480**	**11.8**	**−25.0**	**0.990**	**0.3**	**1.0**
130.21	110	359.2	−26.4	0.13	11.4	6.7
135.92	410	19.9	−25.7	0.13	7.3	2.3
157.96	131	5.9	−28.9	0.26	6.4	2.9
180.22	**1300**	**11.7**	**−25.7**	**0.988**	**0.5**	**0.9**
221.92	310	7.1	−26.8	0.50	4.5	1.5
262.17	350	16.3	−25.9	0.31	4.1	1.3
276.87	530	12.8	−27.2	0.73	2.1	1.0
284.05	**1700**	**11.0**	**−25.0**	**0.999**	**0.9**	**0.4**
357.32	350	17.5	−30.9	0.14	7.5	2.6
471.16	140	10.1	−21.5	0.75	4.2	2.8

Extended Data Fig. 2 | List of selected events. We highlight those with high probability (>90%) to be associated with the LAT-detected source, according to the likelihood analysis. The uncertainty on the estimated γ-ray energies is of the order of 10%. The last two columns show the angular distance to the centre of NGC 253 (the Sculptor galaxy) and the 68% containment radius of the PSF.

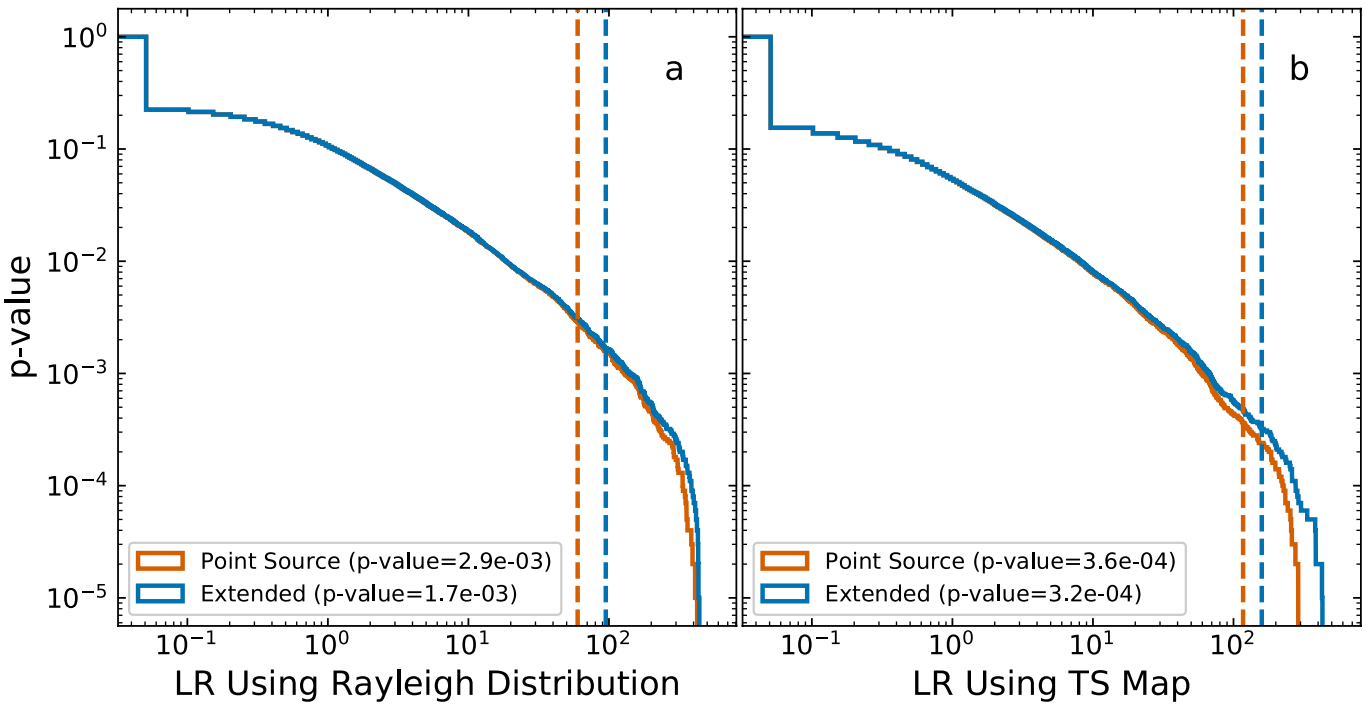

Extended Data Fig. 3 | Distribution of likelihood ratio (LR) values. LR values for 10^5 simulated ROIs using the standard Rayleigh formula (**a**) and using the TS map to compute the probability (**b**). The red distributions correspond to the point source hypothesis, while the blue distributions take into account of the galaxy extension. The step in the distributions at low LR is due to many low-LR trials occupying the first bin. The values of the LRs associated with the Sculptor galaxy are highlighted by red and blue vertical dashed lines for the two cases.

Analysis	p-value	FAR (yr^{-1})
Spatial Association with the Sculptor galaxy		
LR (Rayleigh)	2.9×10^{-3}	4.7×10^{-3}
LR_{ext} (Rayleigh)	1.7×10^{-3}	2.9×10^{-3}
LR (TS Map)	3.6×10^{-4}	6.0×10^{-4}
LR_{ext} (TS Map)	3.2×10^{-4}	5.4×10^{-4}
Temporal Association with GRB 200415A		
Triplet Analysis	8.3×10^{-7} (Li & Ma)	1.6×10^{-7}
Bayesian Blocks	2.3×10^{-3} (Poisson)	6.3×10^{-8}

Extended Data Fig. 4 | Association probability and false alarm rate. Summary of the probability for a random association with the Sculptor galaxy and with the GRB 200415A.

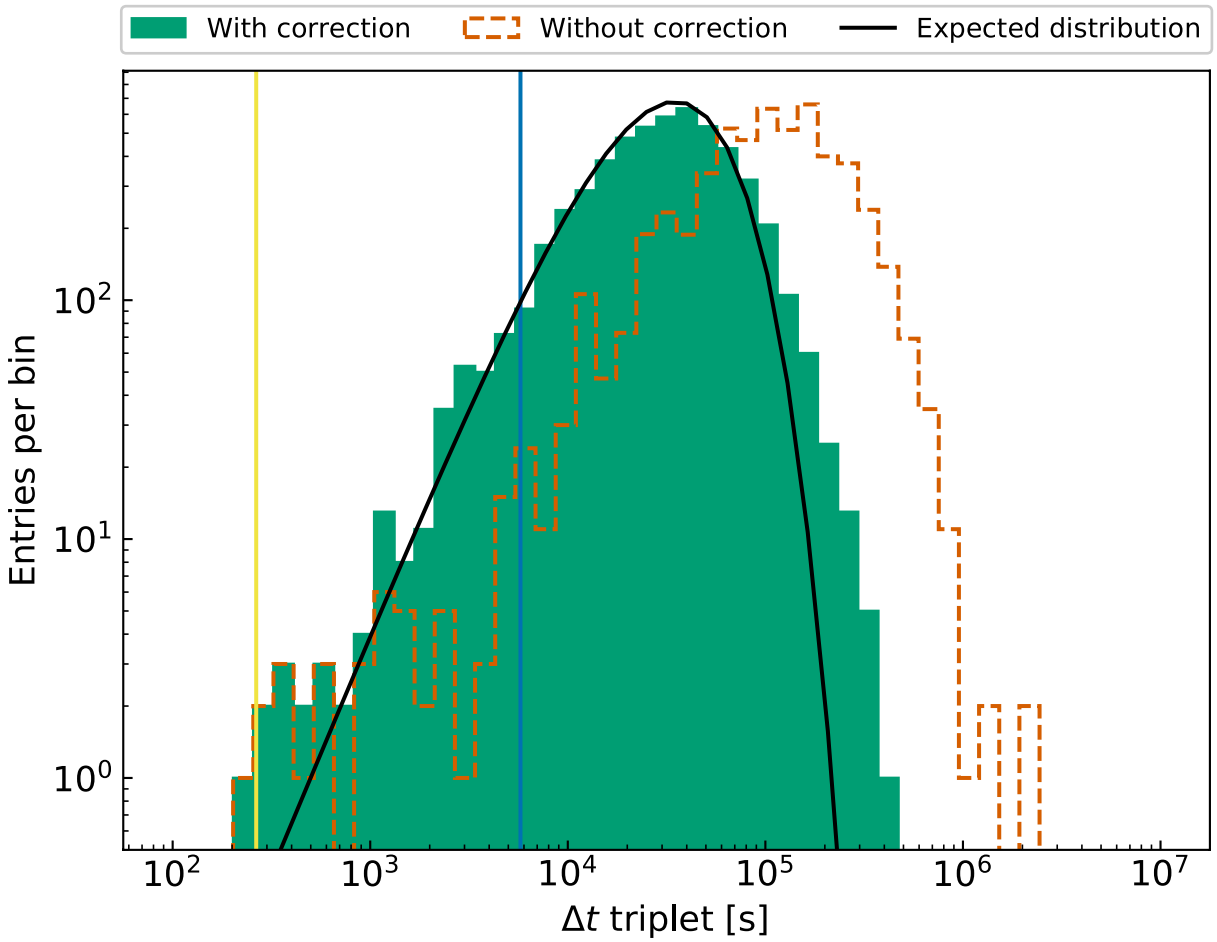

Extended Data Fig. 5 | Triplet distribution. Distribution of the time intervals Δt for triplets formed by three consecutive photons with (green) and without (dashed red) taking into account the correction for the effects of the LAT orbit and FOV. The expected distribution in case of independent events is represented as a solid black line. The vertical line in blue shows the period of the Fermi orbit (5,790 s), while the yellow vertical line indicates $\Delta t = 264.87$ s corresponding to the photon triplet detected by the LAT after GBM detected emission from GRB 200415A.

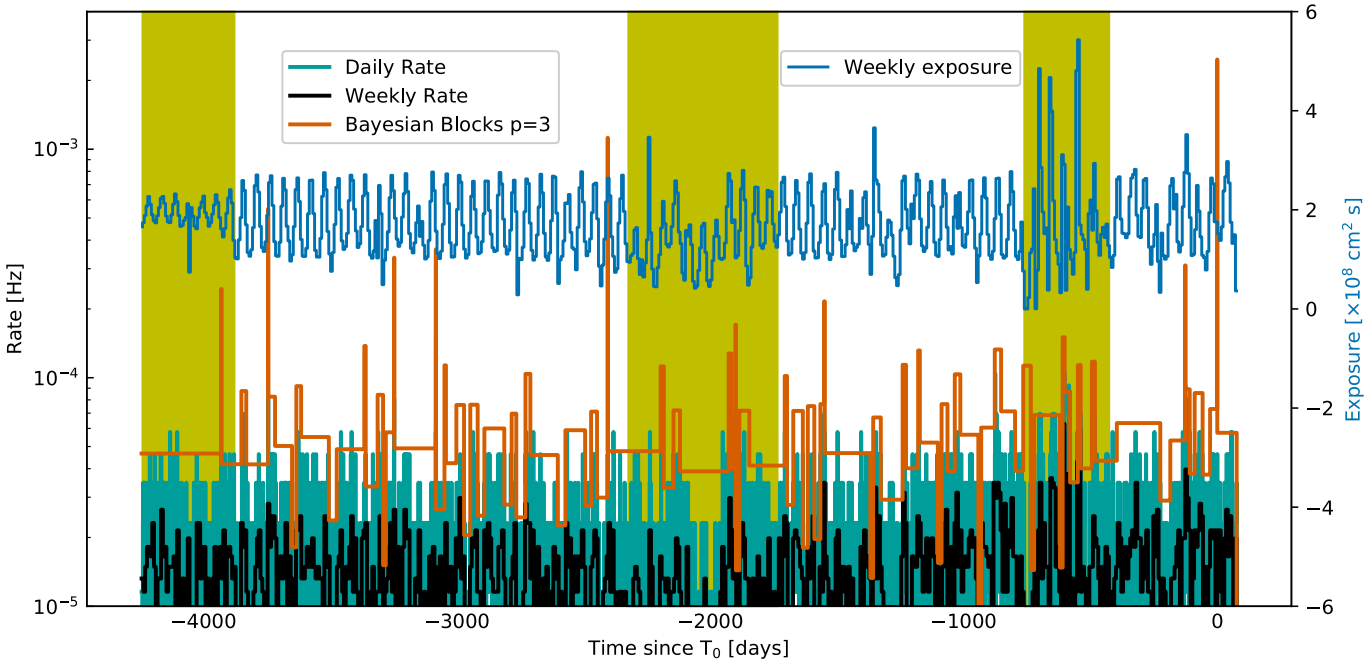

Extended Data Fig. 6 | Rate and exposure as a function of time. Bayesian blocks representation of the arrival times of the γ rays with the prior parameter $p=3$ (red). Light green and dark gray are the daily and weekly count rates, while the blue curve shows the weekly-averaged exposure (between 100 MeV and 300 GeV, assuming a power-law photon index of −2) for a 1°-radius ROI in the direction of Sculptor for the entire time of the mission. Values of the exposure, in units of 10^8 cm^2 s, can be read from the right y-axis. The three yellow bands highlight three characteristic observing profiles: 35° rocking angle, at the beginning of the mission, an observation strategy favouring the Galactic Centre region, in the middle, and, lastly, the period between the start of the solar drive anomaly and the implementation of a reoptimized survey strategy.

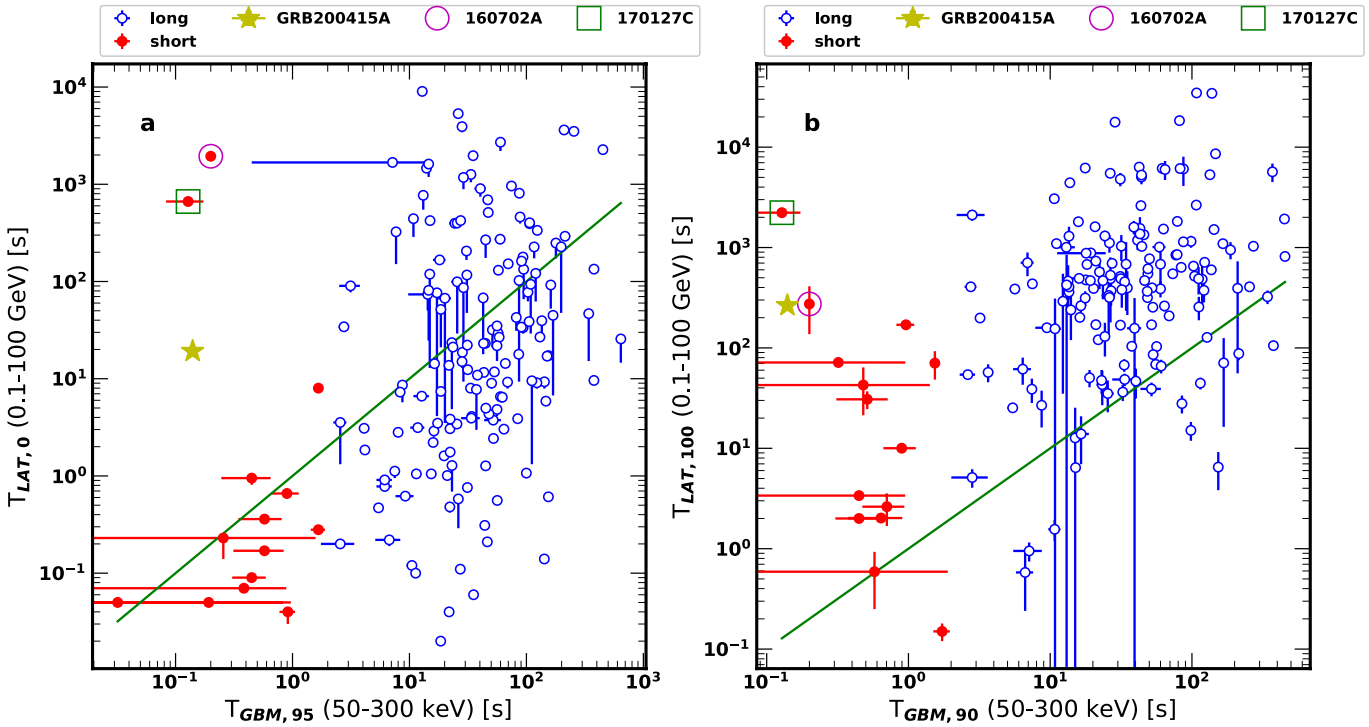

Extended Data Fig. 7 | Comparison with the second Fermi-LAT GRB catalogue. a, Onset times ($T_{LAT,0}$) in the 100 MeV–100 GeV band versus the end of the GRB as detected by GBM in the 50–300 keV energy range ($T_{GBM,95}$). **b**, Durations ($T_{LAT,100}$) calculated in the 100 MeV–100 GeV energy range versus the same quantities calculated in the 50–300 keV energy range ($T_{GBM,90}$). The solid line denotes where the two values are equal. Empty Blue and filled red circles represent long and short GRBs, respectively (data from 2FLGC[27]). GRB 200415A is added and marked with a yellow star. The two SGRBs 160702A and GRB 170127C from 2FLGC, which exhibit similar durations, are highlighted with a magenta circle and green square, respectively.